

Differentiable graph-structured models for inverse design of lattice materials

Dominik Dold^{*,1}, Derek Aranguren van Egmond^{*,1}

¹European Space Agency, Advanced Concepts Team, Noordwijk, The Netherlands

* Both authors contributed equally to this work.

Abstract—Materials possessing flexible physico-chemical properties that adapt on-demand to the hostile environmental conditions of deep space will become essential in defining the future of space exploration. A promising venue for inspiration towards the design of environment-specific materials is in the intricate micro-architectures and lattice geometry found throughout nature. However, the immense design space covered by such irregular topologies is challenging to probe analytically. For this reason, most synthetic lattice materials have to date been based on periodic architectures instead. Here, we propose a computational approach using a graph representation for both regular and irregular lattice materials. Our method uses differentiable message passing algorithms to calculate mechanical properties, and therefore allows using automatic differentiation to adjust both the geometric structure and attributes of individual lattice elements to design materials with desired properties. The introduced methodology is applicable to any system representable as a heterogeneous graph, including other types of materials.

I. INTRODUCTION

Materials used to build future space infrastructure, especially those built directly on other planetary bodies, will require demanding, environment-specific material properties while being relatively easy to process and shape [1]. The constraints imposed by local planetary resources limit the palette of material composition that engineers can exploit to meet desired performance. Much like in nature, engineers will thus come to rely on the optimisation of a material’s topology in addition to its chemical makeup in order to achieve the desired properties under the limitations of the local milieu. Here on Earth, bone, plant stems, dragonfly wings, coral, and radiolarians [2] are just some examples of natural lattice materials that showcase how intricate architecture is used to achieve extreme mechanical performance with a limited choice of constituents [3]. Enhancements in e.g. strength, stiffness, impact toughness, fluid transport, and thermal insulation are all found while conserving light weight and minimizing mass transport. Moreover, an understanding of topological features often unlocks deformation modes and damage tolerant mechanisms not achieved by the bulk material alone.

Inspired by this, synthetic truss-based lattice materials - a subset of so-called Architected Materials - comprise a highly active area of research in materials science. This activity is largely owed to the emergence of modern digital design and fabrication tools like 3D printing, or more formally, additive manufacturing. At the European Space Agency (ESA), capabilities for 3D printing lattice materials from a variety of space-relevant polymers, metals and in-situ planetary regoliths

have been pioneered over the past decade [4], [5]. The geometric freedom afforded by this technology, however, also creates an overwhelming design space of possible topological features, much like in nature. Human engineering has not been afforded the same evolutionary timescales as the natural optimisation pathways that drive biology’s architectures. As such, the complete lattice material design space cannot be explored by engineering intuition alone.

An emergent stream in computational materials science literature is demonstrating high potential for machine learning (ML)-driven design to aid engineers in the exploration of chemical and topological landscapes. Recent years have seen unprecedented demonstrations of physics-informed learning models capable of high fidelity material property predictions based on atomic-level interactions. Key among them are e.g. the deployment of graph neural networks (GNNs) to demystify previously unsolved phase transition dynamics in glassy systems [6], and the use of generative adversarial networks (GANs) and variational autoencoders (VAEs) to predict complex molecular topologies in crystalline nanoporous materials like zeolites and metal-organic frameworks [7], [8].

Along with these developments, research into mechanical metamaterials has also pivoted towards ML as a means to augment the engineer’s intuition with a data-driven geometric design language [9]–[18]. Conventionally these mechanical lattice materials are only formed from periodically repeating unit cells, as this makes their properties addressable analytically and via numerical homogenization in finite element (FE) based simulations. While powerful, homogenization assumes uniformity of lattice properties throughout the global material, and does not account for e.g. local imperfections, stress concentrations and edge-effects from partially constrained unit cells.

Inverse design – the prescription of desired target properties and optimisation over various candidate microstructures – has taken off as a vehicle for ML-aided simulations. Whether supervised (data-driven) [19] or unsupervised (physics-driven) [20], these ML-based prediction models more accurately determine lattice mechanics, and dramatically accelerate the search for candidate architectures that meet target mechanical properties by forgoing computationally expensive FE meshing and conventional Topology Optimisation pathways [21]. In particular, GNNs trained on unit cell structures have recently been proposed to predict mechanical properties of the emergent (periodic) metamaterial in a quick and computationally

economic way [22].

Contrary to periodic lattice materials used for lightweighting (such as hexagonal honeycombs), irregular architected materials – similar to those found in nature – have been shown to boast extraordinary damage tolerance [23], anisotropic functional grading [24] and other surprising properties emerging from local defects and aperiodicity. Control over the most mechanically ‘beneficial’ features of these irregular tilings must happen at local defects and cannot be exerted analytically [25], leaving a near-infinite space of heterogeneous geometric combinations not easily modelled. For this reason, most modern synthetic lattice designs have been restricted to periodic structures, leaving out an ever-growing design space whose potential remains untapped.

We propose a graph-based numerical approach for characterising and inverse-designing emergent properties of lattices with irregular geometries. Inspired by recent work [22], the core idea of our methodology is to represent lattice materials as heterogeneous graphs and perform computations directly on the topology of this graph using an operation called ‘message passing’. This enables a seamless flow of material property information from local features (e.g. between 2 nodes) up to the global lattice, thereby linking effective mechanical properties of the superstructure to local defects in a differentiable way. More specifically, using message passing, we construct a differentiable forward model to predict mechanical properties of lattice materials. The forward model is then used in reverse through the application of automatic differentiation to change local lattice properties – such as beam existence or characteristics of individual beams – until a lattice with a set of desired global mechanical properties has been found (Fig. 1). Thus, the proposed framework enables real-time structural feedback and inverse design for arbitrary lattices, including complicated irregular topologies as found in natural materials.

In the following, we first provide a brief description of the methods used to model and characterize lattice materials. Afterwards, we introduce the general idea of our proposed inverse design methodology, which we denote as ‘differentiable lattices’ in the following. Finally, two realizations of differentiable lattices will be presented, one based on an exact finite element method and one using an approximate model, i.e., a GNN trained on simulated data. Our initial focus is on two-dimensional lattices for simplicity, though the methodology is easily transferred to three-dimensionally architected designs.

II. METHODS

The most important concepts to follow this paper as well as the used mathematical notation are described in the following sections. Detailed descriptions, e.g., on software implementations, can be found in the Supplementary Information.

A. Notation and units

In general, sets are denoted using calligraphic letters, vectors using bold letters and matrices and scalars using normal letters. We summarise a lattice \mathcal{L} as a tuple $\mathcal{L} = (\mathcal{X}, \mathcal{E}, \mathcal{A}_E)$

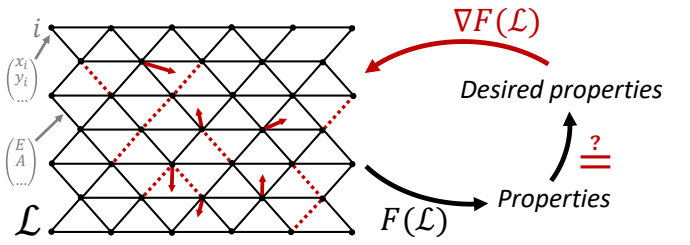


Fig. 1. Schematic illustration of the proposed framework. A lattice material is represented as a graph \mathcal{L} (left) which contains vector attributes both on the nodes (e.g. position) and edges (e.g. Young’s modulus and beam cross-area). A differential forward model F takes the graph as input and predicts material properties. Comparing these predictions with desired properties, automatic differentiation is used to change the material (e.g., move nodes and remove or add beams) to better satisfy those properties. This process is repeated iteratively until a material with the desired properties is found.

consisting of node coordinates $\mathbf{r}_i = (x_i, y_i) \in \mathcal{X}$ for each node i , the set of edges (beams) \mathcal{E} between nodes, e.g., $(i, j) \in \mathcal{E}$ if an edge exists between nodes i and j , and edge attributes $\mathbf{a}_{ij} \in \mathcal{A}_E$. For instance, lattice beams are characterized¹ by their Young’s Modulus E , cross-sectional area A and second moment of area, I . Thus, for a homogeneous lattice, we would set $\mathbf{a}_{ij} = (E, A, I) \forall (i, j) \in \mathcal{E}$.

Distances between nodes are given by $\mathbf{r}_{ij} = \mathbf{r}_j - \mathbf{r}_i$. The length and orientation of a beam between nodes i and j is given by [26]

$$L_{ij} = \sqrt{(x_j - x_i)^2 + (y_j - y_i)^2}, \quad (1a)$$

$$s_{ij} = \frac{y_j - y_i}{L_{ij}}, \quad (1b)$$

$$c_{ij} = \frac{x_j - x_i}{L_{ij}}. \quad (1c)$$

In the following, we abbreviate $L = L_{ij}$, $s = s_{ij}$ and $c = c_{ij}$. For simplicity, we assume that all lattices reside within a normalised bounding box with height b_y and width b_x .

In general, the proposed approach can be used for microscopic as well as macroscopic lattice structures. Here, we report results for a chosen set of material input parameters, with $E = 2$ GPa, $b_x = b_y = 1$ cm and $A = 2 \cdot 10^{-5}$ cm².

For matrices, the index notation $a:b$ denotes the range of integers from a to b , i.e., $K_{0:3}$ is the sub-matrix of K consisting only of its first three rows. We further introduce the specific index notation $\tilde{K}_{ij} = K_{3:i:3:i+3,3:j:3:j+3}$, where the sub-selection is applied to both rows and columns.

B. Modelling 2D lattice materials

To develop a general geometric model for lattice materials, we set out from the simplified case of a 2D lattice material, similar to a honeycomb sandwich panel used commonly in various engineering applications. To model in-plane mechanical properties we employ the direct stiffness method – a finite element matrix method derived from static analysis – to model elastic properties of our lattice material [27]. In it, a lattice is

¹Which, in principle, could be chosen differently for each beam in the lattice. For simplicity, we choose one global value for all beams here.

treated as a collection of connected beams, where each beam between nodes i and j is characterized by its stiffness matrix K_{ij} . The stiffness equation

$$K_{ij} \begin{pmatrix} \mathbf{u}_i \\ \mathbf{u}_j \end{pmatrix} = \begin{pmatrix} \mathbf{F}_i \\ \mathbf{F}_j \end{pmatrix}, \quad (2)$$

allows us to calculate the reaction of the beam element to a given load. Here, $\mathbf{u}_i = (u_i^x, u_i^y, u_i^\varphi)$ are the resulting node displacements due to external forces and moments $\mathbf{F}_i = (F_i^x, F_i^y, M_i^\varphi)$; and φ characterises the resulting bending of beam elements. In this work, we use generalized Euler-Bernoulli beam elements that can both deform along and perpendicular to their longitudinal axis. The stiffness matrix K_{ij} of this generalized beam element is obtained by combining the stiffness matrices of rod elements K_{ij}^{rod} and Euler-Bernoulli beam elements K_{ij}^{EB} ,

$$K_{ij} = K_{ij}^{\text{rod}} + K_{ij}^{\text{EB}}. \quad (3)$$

Rod elements are used here to model the deformation of lattice elements along their longitudinal axis. Their corresponding stiffness matrix is given by [26]

$$K_{ij}^{\text{rod}} = \frac{EA}{L} \begin{pmatrix} c^2 & cs & 0 & -c^2 & -cs & 0 \\ cs & s^2 & 0 & -cs & -s^2 & 0 \\ 0 & 0 & 0 & 0 & 0 & 0 \\ -c^2 & -cs & 0 & c^2 & cs & 0 \\ -cs & -s^2 & 0 & cs & s^2 & 0 \\ 0 & 0 & 0 & 0 & 0 & 0 \end{pmatrix}. \quad (4)$$

Euler-Bernoulli beam elements model the bending of beam elements where the beam length is much larger than the characteristic dimension of the cross section, for which the stiffness matrix is given by [26]

$$K_{ij}^{\text{EB}} = \frac{EI}{L^3} \begin{pmatrix} 12s^2 & -12sc & -6Ls & -12s^2 & 12sc & -6Ls \\ -12sc & 12c^2 & 6Lc & 12sc & -12c^2 & 6Lc \\ -6Ls & 6Lc & 4L^2 & 6Ls & -6Lc & 2L^2 \\ -12s^2 & 12sc & 6Ls & 12s^2 & -12sc & 6Ls \\ 12sc & -12c^2 & -6Lc & -12sc & 12c^2 & -6Lc \\ -6Ls & 6Lc & 2L^2 & 6Ls & -6Lc & 4L^2 \end{pmatrix}. \quad (5)$$

We assume beam elements with a square-shaped cross-sectional area, which corresponds to $I = \frac{bh^3}{12} = \frac{t^4}{12} = \frac{A^2}{12}$, where b, h denote cross-section depth and height, respectively. In a square beam, these are both equal to beam thickness, t [28].

The global stiffness matrix G for the whole lattice (i.e., more than two nodes) is constructed by summing up the contributions of each individual stiffness matrix for every node. This can be achieved iteratively: first, start with G being the zero-matrix (i.e., all elements are zero). Then, for each

beam connecting two nodes i and j in the lattice, G is updated as follows (with $k = K_{ij}$ here):

$$\tilde{G}_{ii} \leftarrow \tilde{G}_{ii} + \tilde{k}_{00}, \quad (6a)$$

$$\tilde{G}_{ij} \leftarrow \tilde{G}_{ij} + \tilde{k}_{01}, \quad (6b)$$

$$\tilde{G}_{ji} \leftarrow \tilde{G}_{ji} + \tilde{k}_{10}, \quad (6c)$$

$$\tilde{G}_{jj} \leftarrow \tilde{G}_{jj} + \tilde{k}_{11}. \quad (6d)$$

The final stiffness equation for a lattice material with N nodes is then given by

$$G \begin{pmatrix} \mathbf{u}_0 \\ \mathbf{u}_1 \\ \dots \\ \mathbf{u}_{N-1} \end{pmatrix} = \begin{pmatrix} \mathbf{F}_0 \\ \mathbf{F}_1 \\ \dots \\ \mathbf{F}_{N-1} \end{pmatrix}. \quad (7)$$

C. Characterising 2D lattice materials

A variety of mechanical in-plane properties are available to characterize the behaviour and functionality of 2D lattice materials. In this work, we focus on the relative density $\bar{\rho}$, effective elastic modulus E^* and Poisson's ratio ν^* . The asterisk denotes ‘‘effective’’ material properties for the entire lattice material (i.e. a global response, not just individual beams).

1) *Relative density*: The most influential design parameter on the in-plane mechanical properties of a cellular lattice material is its relative density, $\bar{\rho} = \frac{\rho^*}{\rho_s}$ [29]. This is defined as the ratio between the lattice's density and the density of the parent solid material, ρ_s . For most practical scenarios, this ratio is equal to the material volume fraction contained within a known bounding box, following the relation:

$$\bar{\rho} = \frac{\rho^*}{\rho_s} = \frac{V_s}{V_{\text{tot}}} = \frac{L^* \cdot t}{b_x \cdot b_y}, \quad (8)$$

where $L^* = \sum_{(i,j) \in \mathcal{E}} L_{ij}$ is the sum of all beam lengths, $t = \sqrt{A}$ the beam thickness (and width) and b_y and b_x the height and width of the bounding box, respectively.

In cases where the bounding box is not known or considered, the relative density of common periodic lattices can also be determined analytically. Table I lists the relative density as a function of beam thickness, t , and regular beam length, L for various periodic regular tilings. Note that, due to the emergence of axial shear effects in thicker beams, these analytical relationships are only applicable when $\bar{\rho} < 0.2$ [29].

2) *Effective elastic modulus*: The effective elastic modulus E^* describes how strongly a material resists to externally-induced deformations. In general, E^* is given by the slope of the linear regime of a material's stress-strain curve.

We use the following experimental setup to determine E^* for arbitrary – including regular as well as irregular – 2D lattice materials. First, the material is glued between two plates in y -direction, i.e., we have a top and a bottom plate (Fig. 2). To obtain the stress-strain curve, the top plate is then iteratively pushed downwards to force the top nodes of the lattice to move. This yields different strains, i.e., displacements

Lattice type (2D)	Relative density ($\bar{\rho}$)	Eff. elastic modulus (E^*)	Poisson's ratio (ν^*)
Square	$2 \frac{t}{L}$	$\frac{1}{2} \bar{\rho} E_s$	0
Triangular (equilat.)	$2\sqrt{3} \frac{t}{L}$	$\frac{1}{3} \bar{\rho} E_s$	$\frac{1}{3}$
Hexagonal	$\frac{2}{\sqrt{3}} \frac{t}{L}$	$\frac{3}{2} \bar{\rho}^3 E_s$	1
Reentrant	$\frac{8}{3\sqrt{3}} \frac{t}{L}$	$\frac{81}{128} \bar{\rho}^3 E_s$	-1

TABLE I
ANALYTICAL RELATIVE DENSITY, EFFECTIVE ELASTIC MODULUS AND
POISSON'S RATIO FOR VARIOUS COMMON 2D LATTICE GRIDS.[29]–[31]

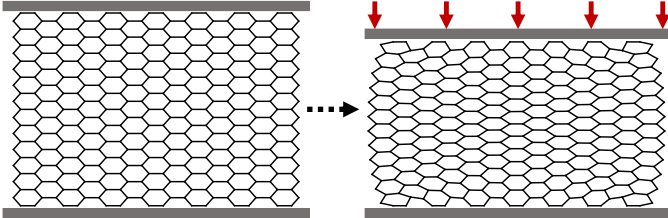


Fig. 2. Experimental setup for determining both the effective elastic modulus and the Poisson's ratio of a lattice material.

in y-direction. The stress is then obtained by measuring what force the material is applying on the top plate in response to the induced displacements. After collecting several stress values for increasing strains, the effective elastic modulus is given by the slope of the resulting stress-strain curve. How this experimental setup translates into simulations in detail is described in Supplementary Information A1. In general, it requires constructing the global stiffness matrix G , applying constraints and deformations, solving the stiffness equation for u_i and updating the node coordinates r_i for all nodes i – which has to be repeated several times to record the stress-strain curve.

For regular grids in 2D, E^* can again be obtained analytically (see Table I). We use this to test our numerical approach, confirming that both analytical and numerical values for E^* agree for regular square, equilateral triangular, honeycomb and reentrant honeycomb lattices with differing relative densities (Fig. 3, left).

3) *Poisson's ratio*: The Poisson's ratio measures how the width of a material changes due to a forced compression of its height. For instance, many materials will widen when compressed, which corresponds to a positive Poisson's ratio. However, so-called auxetic materials do the opposite: when compressed, their width is reduced as well, which corresponds to a negative Poisson's ratio. If the width of the material does not change at all, its Poisson's ratio is 0.

The Poisson's ratio can be obtained with a similar experimental setup as the effective elastic modulus, just that we measure the change in width due to a strain in y-direction. Hence, the Poisson's ratio is given by the slope of a strain-strain curve, as explained in detail in Supplementary Information A2. The width change is calculated by taking the difference of the mean u_r^x value of all nodes on the outer right surface and

the mean u_l^x value of all nodes on the outer left surface of the material. As for the other properties, the Poisson's ratio can be determined analytically for the special case of regular grids (see Table I), which agrees well with our numerically obtained values (Fig. 3, right).

D. Simulation code

This publication is accompanied with an extensive Python module (based on pyTorch) for analysing and designing 2D lattices called *pyLattice2D* (see Supplementary Information B), which is publicly available on gitlab [32]. It contains all experiments performed in this work, as well as many convenience functions, e.g., for the comfortable generation of various 2D lattice geometries. Details on all simulations can further be found in Supplementary Information C.

III. RESULTS

In the following, we first introduce the general framework based on graph-based methods for inverse designing lattice materials. Consequently, we demonstrate two different realizations of this framework: one using exact direct stiffness, and one using GNNs trained on experimental data.

A. Differentiable lattices

1) *Representing lattices as graphs*: Lattices lend themselves to being modelled as graphs, with edges representing beams and nodes representing the locations where beams connect with each other. This allows an efficient and expressive description of lattices, where additional information such as node coordinates, beam cross-area, and beam Young's modulus can be encoded as node and edge features (i.e., real-valued vectors stored on nodes and edges) – something that is not possible when representing lattices as, e.g., images.

2) *Message passing algorithms*: A recent and widely adopted approach of performing calculations on graph-structured data is message passing [33]–[35]. Message passing describes information flow between nodes that are directly connected with an edge, meaning that calculations are performed on edges with stored feature vectors that are locally available to that edge. Usually, operations using message passing can be decomposed into two steps: a *messaging* step and a *reduction* step (Fig. 4). In the messaging step, node features are sent along edges, where they are combined with edge features (and other node features) to calculate new edge features. In the reduction step, newly calculated edge features are sent to neighbouring nodes and combined to form new node features. These operations are performed on all edges and nodes in parallel, allowing efficient and scalable computations on the graph structure itself. Most importantly, this realizes differentiable operations on the discrete structure of the graph, allowing us to utilize gradient-descent based optimization to, e.g., change initial features or even the structure of the graph itself to change the output of the calculation implemented by message passing. This is enabled due to computations following the structure of the graph, i.e., all operations are differentiable, but the sequence of operations (i.e., how and

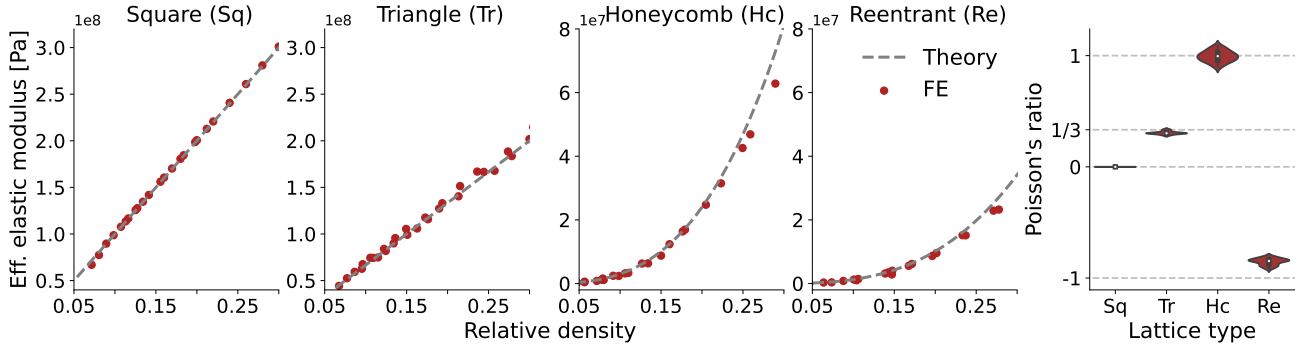


Fig. 3. Comparison of analytical values (Table I) and values obtained using our finite element method (Sections II-B and II-C). To change the relative density, we repeated experiments for lattices with different number of cells and beam cross-areas.

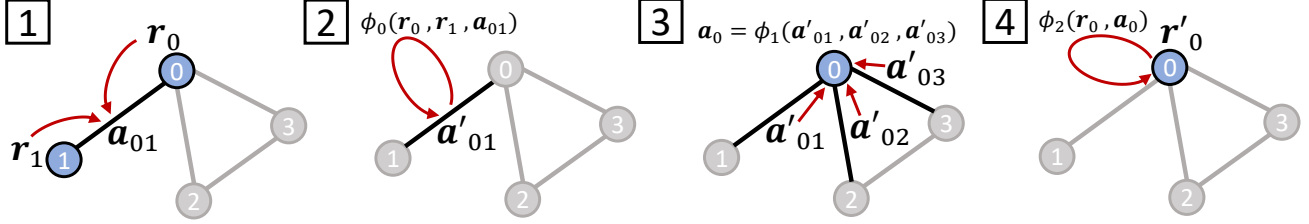


Fig. 4. Illustration of the message passing steps. For clarity, we only show the operations on one edge, although in practice, these operations are performed on all edges in parallel. (1) Node features \mathbf{r}_i are propagated along connecting edges. (2) On the edges, propagated node features as well as edge features are combined via a function ϕ_0 to create new edge features. ϕ_0 can take any shape (e.g., a neural network). (3) Edge features are reduced using a function ϕ_1 that satisfies permutation invariance (i.e., the order of arguments does not matter) and is applicable to a varying number of arguments. (4) The node features are updated using the reduced edge features using a function ϕ_2 (which, again, can take any shape).

which features are combined) is determined by the connectivity of the graph.

3) *Differentiable algorithms for inverse design of lattices:* We propose to use differentiable message passing algorithms for property prediction on lattices represented as graphs, which in turn can then be used to realize an iterative inverse design approach using gradient-descent based optimization.

In general, we denote by $F(\mathcal{L}, S)$ a function that takes node coordinates, graph edges and edge attributes $\mathcal{L} = (\mathcal{X}, \mathcal{E}, \mathcal{A}_E)$ as input and returns one or several material properties of interest, e.g., effective elastic modulus, Poisson's ratio or simply the displacement of each node given a certain external distortion. Optionally, F can also take specific constraints S as input, describing which nodes in the lattice are forced or kept fixed. To ease notation, we neglect writing S as an argument of F in the following.

Although F is still ambiguous here, it can take several shapes, as shown later in Section III-B and Section III-C. Generally, F is composed of several message passing steps, followed by pooling operations (combining node features) and usual differentiable operations such as neural networks.

For inverse design, we compare the predicted property $F(\mathcal{L})$ with a desired target value² ζ . How well prediction and target agree is measured using a loss function L , in our case a L1 loss

$$L(F, \mathcal{L}, \zeta) = \|F(\mathcal{L}) - \zeta\|. \quad (9)$$

²Which, if several properties are predicted, takes the form of a vector.

This loss function is used to find a lattice material with the desired target properties by minimizing it using gradient descent, e.g., by iteratively changing the geometry of the lattice (adjusting node positions using $\nabla_{\mathbf{r}_i}$ or removing/adding beams as described in the next subsection) or by changing the material properties of individual beams (i.e., changing edge features such as the cross-area of individual beams). In this work, we restrict ourselves to geometric changes only to find lattices with desired mechanical properties. Gradient descent is implemented using automatic differentiation, which is readily available in current deep learning libraries such as Tensorflow and pyTorch.

4) *Masking edges:* To enable the removal or addition of beams in a lattice using gradient descent, we introduce an approach inspired by [36] where each edge obtains an additional attribute: a mask value $m_{ij} \in \mathbb{R}$ that is used to decide whether a beam is realized in the lattice between nodes³ i and j . In our case, the masking value is turned into a binary decision by applying the Heaviside step function

$$m_{ij}^\theta = \theta(m_{ij}) = \begin{cases} 1, & \text{if } m_{ij} > 0, \\ 0, & \text{otherwise,} \end{cases} \quad (10)$$

which is used to mask away the contribution of an edge during the reduction step – as if it were not present in the lattice ($m_{ij}^\theta = 1$ – beam exists; $m_{ij}^\theta = 0$ – beam does not exist).

In [36], masks are only used to remove edges from a graph, since enabling adding edges between all possible nodes would

³Thus, $\mathbf{a}_{ij} = (E, A, I, m_{ij})$.

be computationally unfeasible. However, in our case, a node can only be connected to a selected few other nodes in its local neighbourhood, since long beams spanning the whole material are not of interest to us. Thus, when starting from, e.g., a triangular lattice, we can add additional beams to neighbouring nodes that are initially masked out, but can be added during the inverse design process. To guarantee that we do not add crossing beams, we have to generate a list $C_{(i,j)}$ that contains, for each edge (i,j) , other edges that would physically cross it. From this, a final mask value

$$M_{ij} = m_{ij}^\theta \cdot \prod_{(n,m) \in C_{(i,j)}} (1 - m_{nm}^\theta), \quad (11)$$

is obtained, which basically unites the two conditions for a beam to be active in the lattice: its mask value has to be greater than 0 and all other beams that would cross it have to be masked out.

During inverse design, both the list of crossing beams as well as the list of locally neighbouring nodes where beams could be introduced can be adjusted, enabling a complete geometric restructuring of the lattice material⁴.

5) *Surrogate gradients*: One problem remains: the decision function for masking, Eq. (10), has a Dirac delta distribution as its derivative, meaning that it vanishes everywhere except at the threshold, $m_{ij} = 0$. This slows down optimization via gradient descent tremendously – a problem that is well known in other areas such as computational neuroscience, where gradient-based learning for spiking neural networks faces the same problem. However, recently, an approach called “Surrogate Gradients” [37], [38] has been introduced that enables robust gradient-based learning of spiking neural networks.

For learning to mask edges in a graph (or beams in a lattice), we apply the same trick: instead of using the Dirac delta function, we substitute it with a surrogate function with non-vanishing parts off the threshold. A multitude of choices exist for surrogate functions. Specifically for this work, we use a mirrored Lorentz function g as in [39]:

$$g(x) = \frac{1}{(\alpha \cdot |x| + 1)^2}, \quad (12)$$

with $\alpha \in \mathbb{R}^+$ being a choosable hyperparameter and $|x|$ being the absolute value of x . If not stated otherwise, we use $\alpha = 1$.

B. Message passing finite element

As a first realization of F , we show how the direct stiffness method (Section II-B) can be realized using message passing to form an end-to-end differentiable pipeline that returns exact mechanical properties given the graph representation of a lattice material.

⁴In this work, for simplicity, we only update the list of crossing beams to ensure valid lattice designs with non-crossing beams.

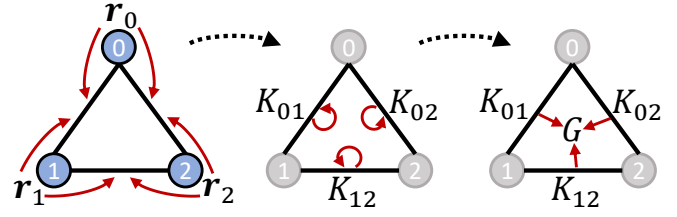


Fig. 5. Illustration of using message passing on the graph representation of the lattice to construct the global stiffness matrix G .

1) *Model*: The direct stiffness approach consists of several steps: (i) constructing the stiffness matrix for each beam, (ii) adding masking to enable optimization of the beam connectivity, (iii) combining those matrices into a global stiffness matrix describing the whole lattice, and (iv) applying the experimental protocol for acquiring the desired mechanical property.

(i) *Stiffness matrices*: For an edge (i,j) , node features \mathbf{r}_i and \mathbf{r}_j (the “messages”) are turned into edge features L_{ij} , s_{ij} and c_{ij} , see Eqs. (1a) to (1c). Those edge features are sufficient to construct the stiffness matrix K_{ij} on the edge, see Eqs. (4) and (5).

(ii) *Masking*: To mask a beam, the binary masking value M_{ij} is multiplied to the stiffness matrix K_{ij} . Hence, if a beam is masked out, its contribution will not appear in the global stiffness matrix.

(iii) *Global stiffness matrix*: Constructing the global stiffness matrix is equivalent to a pooling operation that takes the features (masked stiffness matrix) of each edge and combines it into one global quantity valid for the whole graph (see Fig. 5 for an illustration).

(iv) *Properties*: As discussed in Supplementary Information A1, to calculate the resulting deformation of the lattice given an external load, operations such as selecting parts of arrays and matrices, matrix-vector products, solving a system of linear equations and addition are required, which are all differentiable. Similarly, the additional operations needed to obtain the effective elastic modulus and Poisson’s ratio (e.g. linear regression) are differentiable as well. For the relative density, we can simply sum up L_{ij} , as calculated using message passing in (i), over all edges $(i,j) \in \mathcal{E}$ with $M_{ij} > 0$ to obtain L^* and subsequently $\bar{\rho}$.

Thus, obtaining mechanical properties such as the relative density, resulting node displacements due to a load, effective elastic modulus and Poisson’s ratio can be obtained in a fully differentiable framework, starting with message passing on the graph representation of the lattice, an edge-wise pooling operation and a series of ordinary⁵ differentiable operations.

2) *Experiments*: The described forward model $F(\mathcal{L})$ specifically takes the following information from the graph \mathcal{L} as input: the edge list \mathcal{E} , the masking values $\mathcal{M} = \{m_{ij} \mid (i,j) \in \mathcal{E}\}$ and the node features $\mathcal{X} = \{\mathbf{r}_i \mid 0 \leq i < N\}$ for a lattice with N nodes, $F(\mathcal{L}) = F(\mathcal{X}, \mathcal{E}, \mathcal{M})$. Since it is fully differentiable, it can be used to inverse design a lattice with desired properties using gradient descent. We

⁵I.e., on data without graph structure, such as vectors and matrices.

show this for two scenarios: obtaining a global target property such as a certain effective elastic modulus or Poisson’s ratio, and obtaining a certain deformation given a loading scenario.

Target property: We demonstrate our approach with two examples: starting with a regular honeycomb grid, we inverse design node positions and beam connectivity to acquire a lattice with an effective elastic modulus that is one order of magnitude higher than originally while keeping the relative density $\bar{\rho}$ of the lattice constant (Fig. 6). In addition, we turn an initially regular triangular lattice with positive Poisson’s ratio into a lattice with a negative Poisson’s ratio of $\nu^{\text{target}} = -0.5$, again with the condition of keeping $\bar{\rho}$ unchanged (Fig. 7). In both cases, we start with all edges unmasked⁶ and the used loss function is again a L1 loss with an additional regularization term for the relative density, see Supplementary Information C1 and C2 for details.

In both cases, the required target values are achieved after a small number of iterations. For the honeycomb lattice, the inverse design leads to a restructuring that is more akin to a square lattice, which is expected as square grids have high stiffness. To get a configuration with the same relative density as the initial lattice, beams that only weakly influence E^* are removed after the target elastic modulus has been reached. For the triangular lattice, a configuration is found that, in general, promotes inward bending of elements during compression, resulting in a negative Poisson’s ratio. A peculiar feature are the arc-like structures on the bottom and top of the lattice that promote such inward movements.

Target deformation: In addition to global material properties, we can also inverse design the node displacements of the lattice to a given load. In Fig. 8, a lattice material that can perform a grabbing motion is found through inverse design. In this case, the inverse design creates interesting functional structures, such as a lever-like arrangement (situated in the left bottom corner of the hole in the lattice) that pulls up the bottom-right part of the material when the lattice is compressed.

Additionally, in Fig. 9, we demonstrate that our approach can be used to design a lattice with several target behaviours. For both scenarios, we allow new beams to be added between nodes that were initially not present in the lattice.

Details to both experiments can be found in Supplementary Information C3 and C4.

C. Graph neural networks

Instead of a finite element method, F can also be an approximate model obtained using, e.g., machine learning. This is particularly useful when an analytical treatment is not feasible or only experimental data is available. Recently, GNNs using convolutional operators [33], [35], [40] have reached competitive performance on a variety of graph inference tasks such as link prediction and node classification, translating into applications such as molecule property prediction [41],

⁶I.e., beams that are originally not available cannot be added during inverse design.

mesh-based simulations [42], modelling glassy systems [6], generalized neural algorithm learners [43], as well as material science and chemistry [44]. They are especially interesting due to their property of being able to deal with graphs that have a varying number of nodes as well as carry numerical features on nodes and edges. Hence, in the following, we provide a proof of concept for using GNNs both for predicting the properties of lattice materials as well as inverse designing novel lattices.

1) *Dataset generation:* For training, evaluating and testing GNNs on predicting mechanical properties, we require an extensive dataset. As a proof of concept, we generated simulated data using the direct stiffness method (Section II-B). Lattices with different base tiling (Square, Equilateral Triangle, Honeycomb and Reentrant Honeycomb) and deformations (random node displacements and beam/node removals) have been generated, with 4000, 200 and 1000 lattices of each tiling (train, validation and test data, respectively) – i.e., in total 16000 training, 800 validation and 4000 test samples. A detailed description of these perturbations can be found in Supplementary Information C5, and a visualisation of examples from the training dataset is shown in Fig. 10.

2) *Property prediction:* First, we train models that utilize message passing to predict in-plane material properties of 2D lattices. We investigate two different GNN architectures: (i) GNNs based on the simple EdgeConv layer introduced in [45], as well as a message passing neural network (MPNN) architecture used for molecule property prediction [41]. The model architectures are explained in detail in Supplementary Information D1. For comparison, we further train a linear regression and CatBoost model [46] (i.e., a gradient-boosted tree) on handcrafted features extracted from the lattices such as cell density and relative density (see Supplementary Information D2). As an alternative, focusing only on the geometry of the lattice, we also train a convolutional neural network (CNN) on image representations of the lattices.

To estimate the performance of the models, we report in Table II the root mean squared error (RMSE) calculated on the test set. The best model during training is selected using the validation split. In general, the CNN, CatBoost and MPNN perform similarly, clearly outperforming linear regression. The best performance is reached by the EdgeConv GNN.

More specifically, we found that the models learn to predict the effective elastic modulus from the lattice geometry (or tabular features) very well, while the Poisson’s ratio is much

Model	Eff. elastic modulus	Poisson’s ratio
	RMSE [10^{-2}]	RMSE [10^{-2}]
Lin. Regr.	7.22	23.00
CatBoost	3.17	10.89
CNN	3.01	10.53
EdgeConv	2.61	11.26
MPNN	3.46	10.65

TABLE II
EXPERIMENTAL RESULTS FOR TRAINING PREDICTION MODELS.

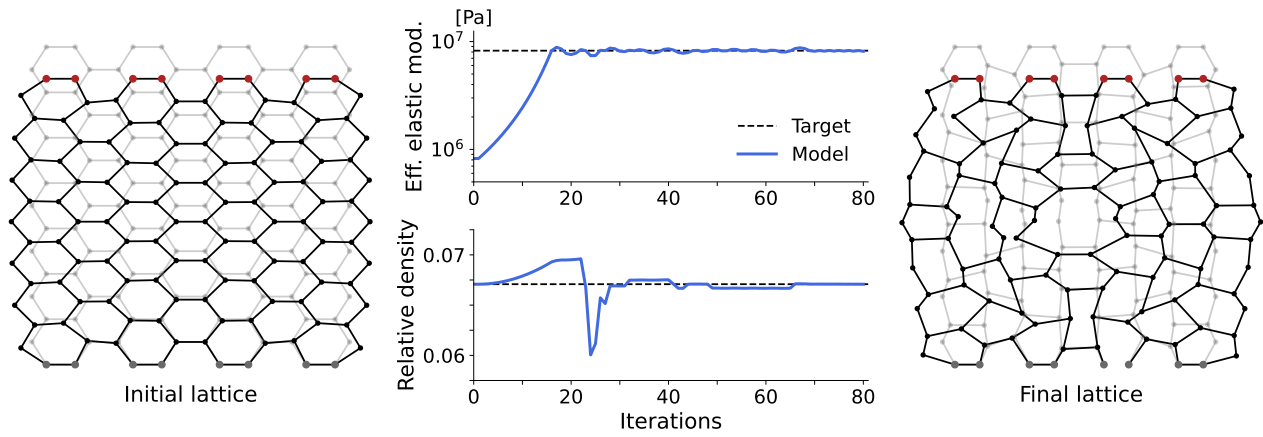


Fig. 6. Inverse designing a square lattice to have a higher effective elastic modulus while keeping the relative density constant. Lattices without load is shown in light gray and with load in black. Top nodes (red) are forced, while bottom nodes (gray) are constrained to not move. Deformations are magnified by a factor of 10.

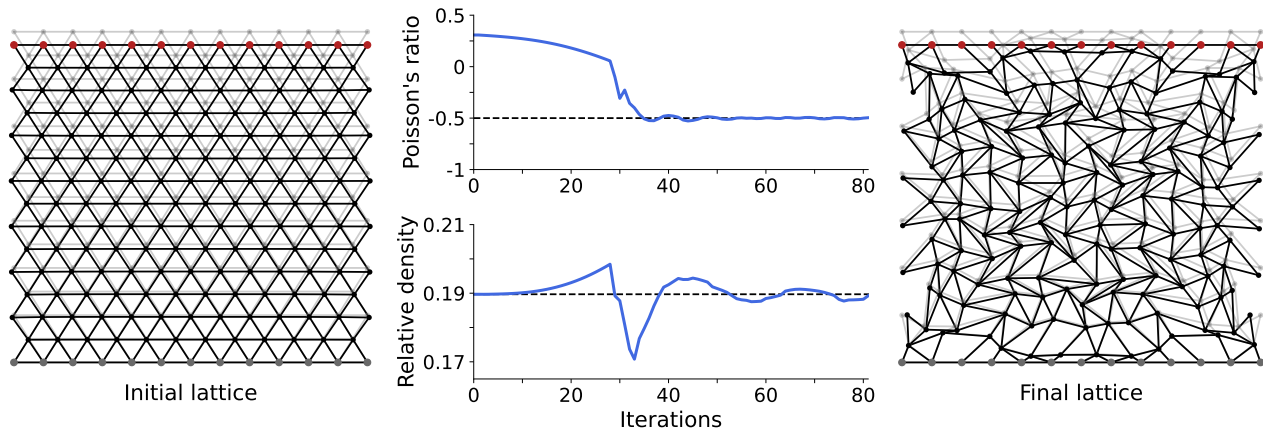


Fig. 7. Inverse designing a triangle lattice to have a negative Poisson's ratio while keeping the relative density constant. Colors and line styles as in Fig. 6.

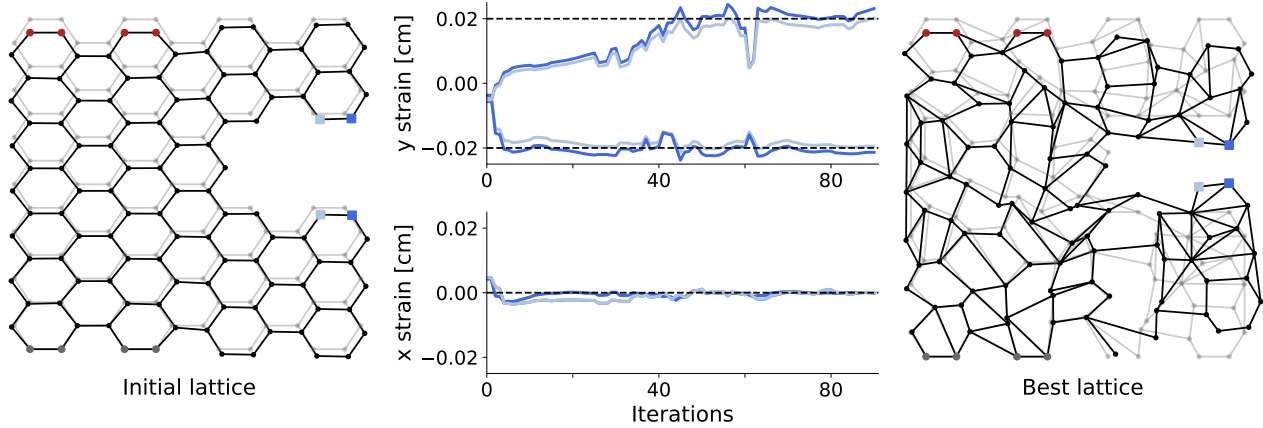


Fig. 8. Inverse designing a lattice to yield a certain deformation response to a load. Here, the top left part of the lattice is squeezed downwards while the bottom left part is kept in place. Initially, this leads to an outward bend of the right part of the lattice, which is turned into a grabbing motion through inverse design. To achieve this, we provide a target deformation in y and x-direction for some of the nodes (squares) in the material's cavity. Colors and line styles as in Fig. 6. Deformations are magnified by a factor of 4.

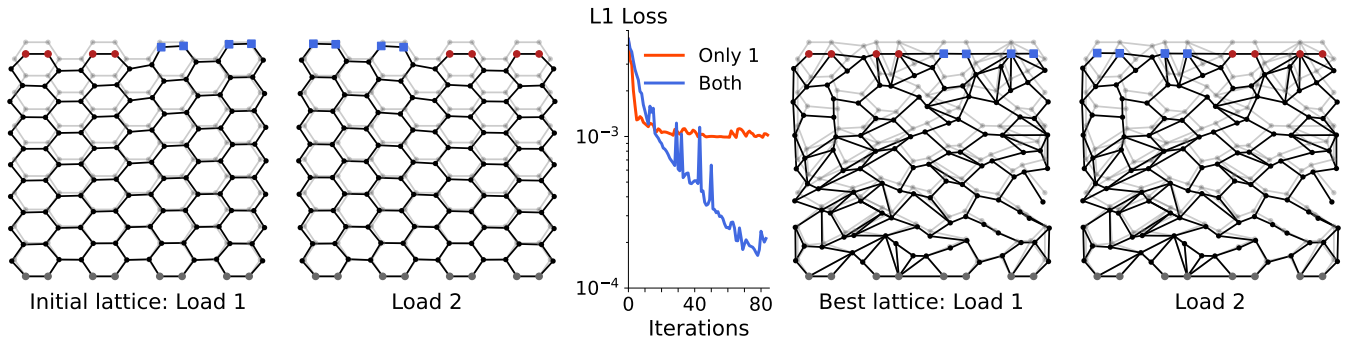


Fig. 9. Inverse designing the response to two different load scenarios. Either the top left part is pushed down while the top right part is free to move (load 1) or vice versa (load 2). As a target behaviour, we aim at keeping the top surface flat. As can be seen in the middle figure, if we only train on load scenario 1, the target behaviour for load scenario 2 is not reached. However, training on both scenarios will lead to a solution that satisfies both target behaviours. Although the target is only provided for one particular load strength, the learned design is valid over a large range of external deformations, see Supplementary Information E1. Colors, line styles and node symbols as in Fig. 8. Deformations are magnified by a factor of 5.

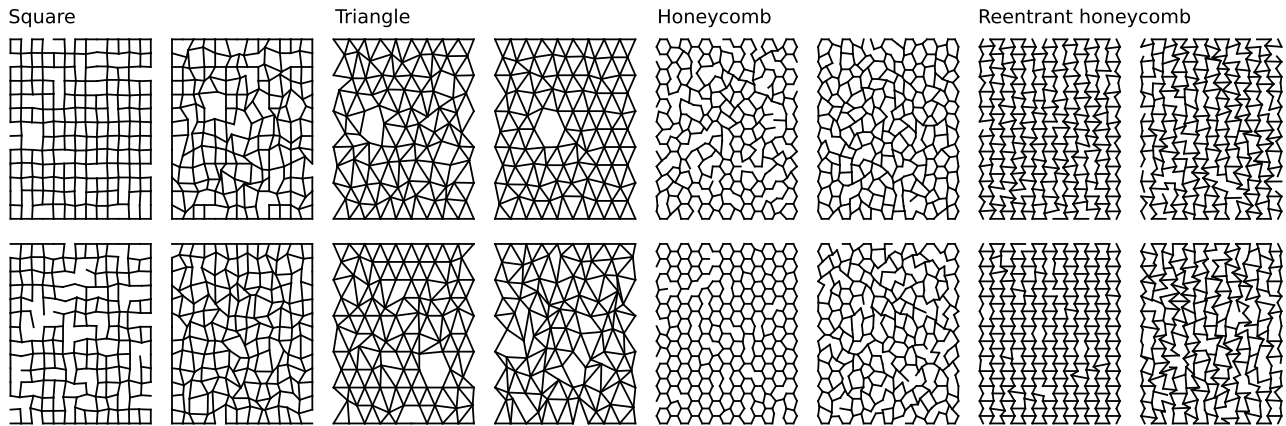


Fig. 10. Example lattices from the generated training dataset.

harder to learn. Especially for square lattices, we found that all models perform rather badly, although good performances are reached for reentrant honeycomb and honeycomb lattices. This is illustrated in Fig. 11, where we compare predicted and experimental values for the EdgeConv GNN. Details on the experiments can be found in Supplementary Information C6.

These are promising results, especially since both GNN architectures are end-to-end differentiable and can thus be used as an approximate replacement of F for the inverse design framework introduced in Section III-B.

3) *Inverse design using graph neural networks:* To showcase the usage of GNNs for 2D lattice inverse design, we use an EdgeConv GNN trained to predict the effective elastic modulus as the forward model F . To enable changing the beam structure of the lattice, we have to properly implement masking of edges in the message passing architecture of the GNN, which is explained in Supplementary Information D3. In Fig. 12, we show that inverse design is possible through a trained model, yielding a lattice design that has the desired target properties. To ensure that the GNN did not simply return a lattice design from the training dataset, we show the two closest lattices from the training data in Supplementary Information E2.

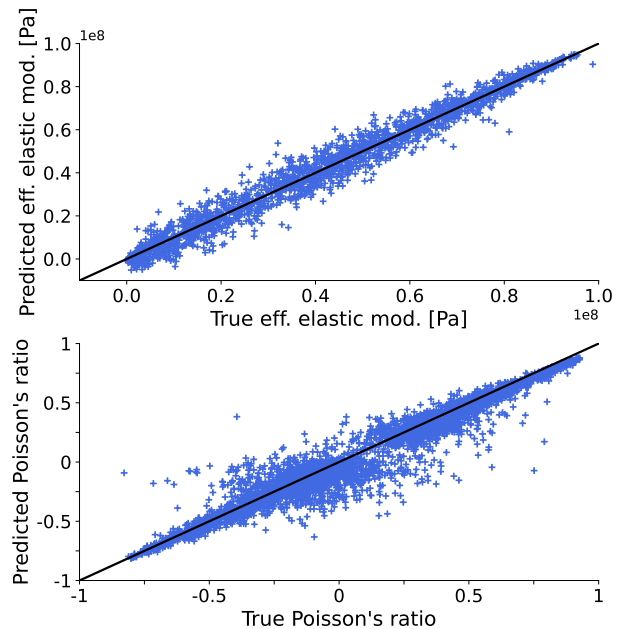


Fig. 11. Model prediction vs. ground truth for the EdgeConv model.

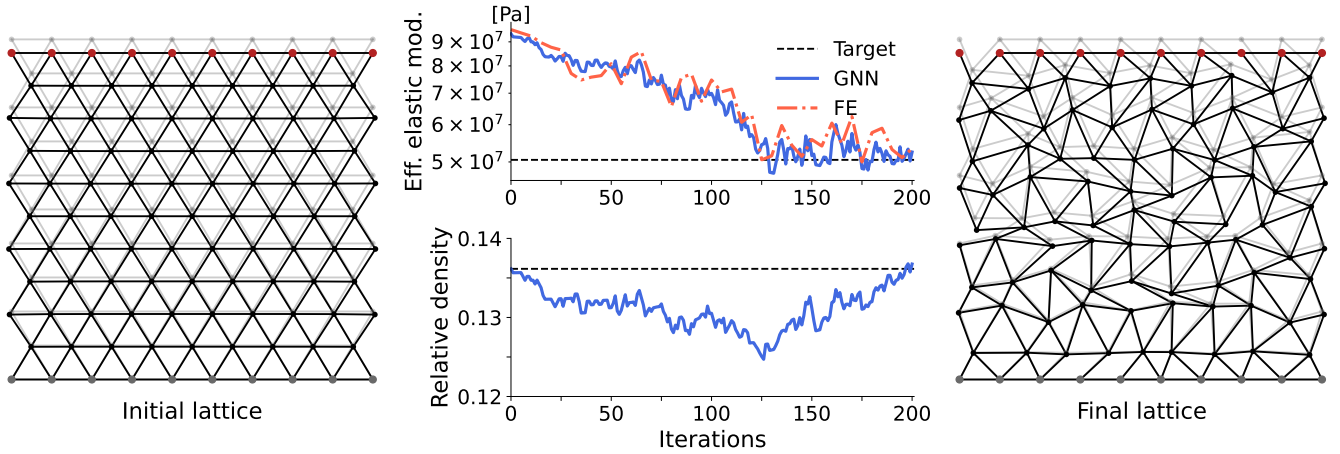


Fig. 12. Inverse design using a GNN as the forward model F . A triangle lattice is adjusted to feature a reduced effective elastic modulus while its relative density has to be unchanged. Target values for the elastic modulus and relative density are shown as dashed lines. The predicted value by the GNN F is shown in blue (straight line), while the exact value obtained using finite element is shown in red (dashed dotted line). Colors and line styles as in Fig. 6. Deformations are magnified by a factor of 2.

Different from inverse design using an exact, analytical forward model (Section III-B), the optimization process is noisier. Furthermore, we found that it works less reliably the further one moves away from the value regime covered during training of the model. In fact, the design loop can get stuck in configurations of the lattice that are not realistic (e.g., disconnected components) without being able to recover from it on its own. Although this can be accounted for in the inverse design framework, for instance by not allowing changes to the geometry that result in unphysical lattice materials, this is a clear downside of the approach compared to using an exact model as in Section III-B.

IV. DISCUSSION

For inverse design, the exact forward model (message passing finite element) has the strong advantage that no training data is required at all. In addition, the presented approach allows additional physical information of the lattice to be encoded as either node or edge features. Thus, the scheme can be generalized to create completely heterogeneous lattices (each beam with different values of E and A) to satisfy a given set of target properties. In fact, due to the model being exact, a complete restructuring of the lattice geometry and its properties is possible without ever leaving the regime where the forward model is valid – unless modifications are made that result in a free-hinged structure or disconnected material. However, the model requires a full finite element implementation that – depending on the size of the material and the degree of realism of the used finite element approach – can be computationally inefficient and slow. Still, as only a few iterations are required to find a single lattice design, we are confident that the approach scales to more complex applications and can be utilized as a design assistant to explore novel, irregular lattice materials.

An alternative to using an exact forward model is training a surrogate model, e.g., GNNs, which is computationally less

demanding than running a finite element simulation. Furthermore, it can be applied to experimentally recorded data and a variety of (non-linear) mechanical properties. In this work, we trained GNNs on predicting the effective elastic modulus E^* and Poisson’s ratio ν^* of lattice materials. Although good performance is reached for predicting E^* , the model struggled with predicting ν^* accurately, especially for small absolute values of ν^* . To better understand the predictive power of GNNs in this application, a higher number of mechanical properties should be investigated in future work, as well as alternative GNN architectures that are more tailored to the problem of lattice material property prediction. Moreover, we only used lattices with a predefined base tiling and small range of cells. In future work, a larger dataset that covers a vast regime of lattice topologies (e.g. based on Voronoi grids) could strongly benefit the training process. Major downsides of using GNNs is that a lot of training data is required – more than might be accessible from experimental observations. In this case, a transfer learning approach might be used, where the model is first trained with simulated data and then fine-tuned, or partially retrained to predict novel properties, using experimental data. Finally, another possibility for reducing the amount of training data required as well as increase the performance and robustness of the model is to use a hybrid approach that integrates part of the analytical model in the GNN, basically molding knowledge about the underlying physics into the GNN architecture.

V. CONCLUSION

We present a framework that utilizes differentiable graph representations of lattices to perform both property prediction and inverse design. The main focus lies hereby on using message passing algorithms, which perform calculations directly on the geometric structure of the lattice’s graph representation and allow the modification of mechanical properties and beam connectivity using automatic differentiation. We show that finite element methods can be realized using message passing,

or GNNs trained on simulated data can act as surrogate models thereof. This yields an efficient and expressive way of both describing and parametrizing lattices as well as modelling their behaviour mathematically.

Our approach constitutes an important step towards enabling automatic inverse design of irregularly structured lattice materials. Moreover, it opens up a new set of tools developed in the graph machine learning literature, such as the GNNExplainer method, for analyzing both regular and irregular lattices. We hope that this will spark new ideas for representing 3D-printable materials and lead to a wealth of novel approaches and tools that assist practitioners in designing new (multi)-functional materials.

Finally, we would like to stress that the approach introduced in this work is not limited to describing lattices, but is applicable to any system that constitutes of a graph representation and a forward model that predicts its properties – thus allowing automatic differentiation to change the structure of the input graph until it satisfies a set of desired properties.

ACKNOWLEDGMENT

We would like to thank Jai Grover and Elissa Ross for helpful and stimulating discussions. We further thank our colleagues at ESA’s Advanced Concepts Team for their ongoing support. Both authors acknowledge support through the European Space Agency fellowship and young graduate trainee programs.

AUTHOR CONTRIBUTIONS

Both authors designed the theoretical and experimental aspects of this study. DD created the pyLattice2D package based on initial code by DAve. Both authors contributed to the pyLattice2D code. DD performed the simulations. Both authors wrote the manuscript based on an initial draft by DD.

DECLARATION OF INTERESTS

The authors declare no competing interests.

REFERENCES

- [1] T. Ghidini, “Materials for space exploration and settlement,” *Nature materials*, vol. 17, no. 10, 2018.
- [2] L. J. Gibson, M. F. Ashby, and B. A. Harley, *Cellular materials in nature and medicine*. Cambridge University Press, 2010.
- [3] U. G. Wegst, H. Bai, E. Saiz, A. P. Tomsia, and R. O. Ritchie, “Bioinspired structural materials,” *Nature materials*, vol. 14, no. 1, 2015.
- [4] A. Makaya, L. Pambaguian, T. Ghidini, T. Rohr, U. Lafont, and A. Meurisse, “Towards out of earth manufacturing: Overview of the esa materials and processes activities on manufacturing in space,” *CEAS Space Journal*, 2022.
- [5] A. Mitchell, U. Lafont, M. Hołyńska, and C. Semprimoschnig, “Additive manufacturing—a review of 4d printing and future applications,” *Additive Manufacturing*, vol. 24, 2018.
- [6] V. Bapst, T. Keck, A. Grabska-Barwińska, C. Donner, E. D. Cubuk, S. S. Schoenholz, A. Obika, A. W. Nelson, T. Back, D. Hassabis, *et al.*, “Unveiling the predictive power of static structure in glassy systems,” *Nature Physics*, vol. 16, no. 4, 2020.
- [7] B. Kim, S. Lee, and J. Kim, “Inverse design of porous materials using artificial neural networks,” *Science Advances*, vol. 6, no. 1, 2020.

- [8] Z. Yao, B. Sánchez-Lengeling, N. S. Bobbitt, B. J. Bucior, S. G. H. Kumar, S. P. Collins, T. Burns, T. K. Woo, O. K. Farha, R. Q. Snurr, and A. Aspuru-Guzik, “Inverse design of nanoporous crystalline reticular materials with deep generative models,” *Nature Machine Intelligence*, vol. 3, no. 11, 2021.
- [9] Y. Mao, Q. He, and X. Zhao, “Designing complex architected materials with generative adversarial networks,” *en, Science Advances*, vol. 6, no. 17, Apr. 2020, ISSN: 2375-2548. DOI: 10.1126/sciadv.aaz4169. [Online]. Available: <https://advances.sciencemag.org/lookup/doi/10.1126/sciadv.aaz4169>.
- [10] A. Challapalli, D. Patel, and G. Li, “Inverse machine learning framework for optimizing lightweight metamaterials,” *en, Materials & Design*, vol. 208, Oct. 2021, ISSN: 0264-1275. DOI: 10.1016/j.matdes.2021.109937. [Online]. Available: <https://www.sciencedirect.com/science/article/pii/S0264127521004913>.
- [11] K. Guo and M. J. Buehler, “A semi-supervised approach to architected materials design using graph neural networks,” *en, Extreme Mechanics Letters*, vol. 41, Nov. 2020, ISSN: 2352-4316. DOI: 10.1016/j.eml.2020.101029. [Online]. Available: <https://www.sciencedirect.com/science/article/pii/S2352431620302418>.
- [12] K. Guo, Z. Yang, C.-H. Yu, and M. J. Buehler, “Artificial intelligence and machine learning in design of mechanical materials,” *en, Materials Horizons*, vol. 8, no. 4, 2021. DOI: 10.1039/D0MH01451F. [Online]. Available: <https://pubs.rsc.org/en/content/articlelanding/2021/mh/d0mh01451f>.
- [13] S. C.-y. Shen and M. J. Buehler, “Nature-inspired architected materials using unsupervised deep learning,” *en, Communications Engineering*, vol. 1, no. 11, Nov. 2022, ISSN: 2731-3395. DOI: 10.1038/s44172-022-00037-0. [Online]. Available: <https://www.nature.com/articles/s44172-022-00037-0>.
- [14] X. Zheng, T.-T. Chen, X. Guo, S. Samitsu, and I. Watanabe, “Controllable inverse design of auxetic metamaterials using deep learning,” *en, Materials & Design*, vol. 211, Dec. 2021, ISSN: 0264-1275. DOI: 10.1016/j.matdes.2021.110178. [Online]. Available: <https://www.sciencedirect.com/science/article/pii/S0264127521007334>.
- [15] X. Zheng, T.-T. Chen, X. Jiang, M. Naito, and I. Watanabe, “Deep-learning-based inverse design of three-dimensional architected cellular materials with the target porosity and stiffness using voxelized voronoi lattices,” *Science and Technology of Advanced Materials*, vol. 24, no. 1, Dec. 2023, ISSN: 1468-6996. DOI: 10.1080/14686996.2022.2157682. [Online]. Available: <https://doi.org/10.1080/14686996.2022.2157682>.
- [16] M. Maurizi, C. Gao, and F. Berto, “Inverse design of truss lattice materials with superior buckling resistance,” *en, npj Computational Materials*, vol. 8, no. 11, Nov. 2022, ISSN: 2057-3960. DOI: 10.1038/s41524-022-00938-w. [Online]. Available: <https://www.nature.com/articles/s41524-022-00938-w>.
- [17] —, “Predicting stress, strain and deformation fields in materials and structures with graph neural networks,” *Scientific Reports*, vol. 12, no. 1, 2022.
- [18] Z. Yang and M. J. Buehler, “High-throughput generation of 3d graphene metamaterials and property quantification using machine learning,” *Small Methods*, vol. 6, no. 9, 2022.
- [19] M. Mozaffar, R. Bostanabad, W. Chen, K. Ehmann, J. Cao, and M. Bessa, “Deep learning predicts path-dependent plasticity,” *Proceedings of the National Academy of Sciences*, vol. 116, no. 52, 2019.
- [20] J.-H. Bastek, S. Kumar, B. Telgen, R. N. Glaesener, and D. M. Kochmann, “Inverting the structure–property map of truss metamaterials by deep learning,” *Proceedings of the National Academy of Sciences*, vol. 119, no. 1, Jan. 2022, ISSN: 0027-8424, 1091-6490. DOI: 10.1073/pnas.2111505119. [Online]. Available: <http://www.pnas.org/lookup/doi/10.1073/pnas.2111505119>.
- [21] J. Gao, Z. Luo, H. Li, and L. Gao, “Topology optimization for multiscale design of porous composites with multi-domain microstructures,” *en, Computer Methods in Applied Mechanics and Engineering*, vol. 344, Feb. 2019, ISSN: 0045-7825. DOI: 10.1016/j.cma.2018.10.017. [Online]. Available: <https://www.sciencedirect.com/science/article/pii/S0045782518305206>.
- [22] E. Ross and D. Hambleton, “Using graph neural networks to approximate mechanical response on 3d lattice structures,” *Proceedings of AAG2020-Advances in Architectural Geometry*, vol. 24, 2021.
- [23] D. A. Aranguren van Egmond, “Designing for disorder: The mechanical behaviour of bioinspired, stochastic honeycomb materials,” *Master’s thesis*, 2018.

- [24] S. Kumar, S. Tan, L. Zheng, and D. M. Kochmann, "Inverse-designed spinodoid metamaterials," *npj Computational Materials*, vol. 6, no. 1, Jun. 2020, ISSN: 2057-3960. DOI: 10.1038/s41524-020-0341-6. [Online]. Available: <https://www.nature.com/articles/s41524-020-0341-6>.
- [25] S. Bonfanti, R. Guerra, F. Font-Clos, D. Rayneau-Kirkhope, and S. Zapperi, "Automatic design of mechanical metamaterial actuators," *Nature communications*, vol. 11, no. 1, 2020.
- [26] A. Öchsner and R. Makvandi, *Finite elements for truss and frame structures: an introduction based on the computer algebra system Maxima*. Springer, 2018.
- [27] J. Bühring, J. Soika, M. Schirp-Schoenen, and K.-U. Schröder, "Elastic axial stiffness properties of lattice structures: Analytical approach and experimental validation for bcc and f2cc, z unit cells," *Mechanics of Advanced Materials and Structures*, 2022.
- [28] T. H. G. Megson, *Structural and stress analysis*. Butterworth-Heinemann, 2019.
- [29] L. J. Gibson and M. F. Ashby, *Cellular Solids: Structure and Properties*, 2nd ed. Cambridge University Press, 1997.
- [30] A.-J. Wang and D. McDowell, "Yield surfaces of various periodic metal honeycombs at intermediate relative density," *International Journal of Plasticity*, vol. 21, no. 2, 2005.
- [31] T.-C. Lim, *Auxetic materials and structures*. Springer, 2015, vol. 11.
- [32] *pyLattice2D*, <https://gitlab.com/EuropeanSpaceAgency/pylattice2d>.
- [33] T. N. Kipf and M. Welling, "Semi-supervised classification with graph convolutional networks," in *J. International Conference on Learning Representations (ICLR 2017)*, 2016.
- [34] J. Gilmer, S. S. Schoenholz, P. F. Riley, O. Vinyals, and G. E. Dahl, "Neural message passing for quantum chemistry," in *International conference on machine learning*, PMLR, 2017.
- [35] W. Hamilton, Z. Ying, and J. Leskovec, "Inductive representation learning on large graphs," *Advances in neural information processing systems*, vol. 30, 2017.
- [36] Z. Ying, D. Bourgeois, J. You, M. Zitnik, and J. Leskovec, "Gnnexplainer: Generating explanations for graph neural networks," *Advances in neural information processing systems*, vol. 32, 2019.
- [37] E. O. Neftci, H. Mostafa, and F. Zenke, "Surrogate gradient learning in spiking neural networks: Bringing the power of gradient-based optimization to spiking neural networks," *IEEE Signal Processing Magazine*, vol. 36, no. 6, 2019.
- [38] F. Zenke and T. P. Vogels, "The remarkable robustness of surrogate gradient learning for instilling complex function in spiking neural networks," *Neural computation*, vol. 33, no. 4, 2021.
- [39] F. Zenke and S. Ganguli, "Superspike: Supervised learning in multi-layer spiking neural networks," *Neural computation*, vol. 30, no. 6, 2018.
- [40] M. Schlichtkrull, T. N. Kipf, P. Bloem, R. Van Den Berg, I. Titov, and M. Welling, "Modeling relational data with graph convolutional networks," in *European semantic web conference*, Springer, 2018.
- [41] C. Lu, Q. Liu, C. Wang, Z. Huang, P. Lin, and L. He, "Molecular property prediction: A multilevel quantum interactions modeling perspective," in *Proceedings of the AAAI Conference on Artificial Intelligence*, vol. 33, 2019.
- [42] T. Pfaff, M. Fortunato, A. Sanchez-Gonzalez, and P. W. Battaglia, "Learning mesh-based simulation with graph networks," *arXiv preprint arXiv:2010.03409*, 2020.
- [43] B. Ibarz, V. Kurin, G. Papamakarios, K. Nikiforou, M. Bennani, R. Csordás, A. Dudzik, M. Bošnjak, A. Vitvitskiy, Y. Rubanova, et al., "A generalist neural algorithmic learner," *arXiv preprint arXiv:2209.11142*, 2022.
- [44] P. Reiser, M. Neubert, A. Eberhard, L. Torresi, C. Zhou, C. Shao, H. Metni, C. van Hoesel, H. Schopmans, T. Sommer, et al., "Graph neural networks for materials science and chemistry," *Communications Materials*, vol. 3, no. 1, 2022.
- [45] Y. Wang, Y. Sun, Z. Liu, S. E. Sarma, M. M. Bronstein, and J. M. Solomon, "Dynamic graph cnn for learning on point clouds," *Acm Transactions On Graphics (tog)*, vol. 38, no. 5, 2019.
- [46] L. Prokhorenkova, G. Gusev, A. Vorobev, A. V. Dorogush, and A. Gulin, "Catboost: Unbiased boosting with categorical features," *Advances in neural information processing systems*, vol. 31, 2018.

A. Details of the direct stiffness approach

1) *Calculating the effective elastic modulus:* For simplicity, we denote by \mathcal{T} the set containing all indices of top nodes (i.e., all nodes forming the top surface of the material) and \mathcal{B} the set containing the indices of bottom nodes.

- 1) First, construct the global stiffness matrix G .
- 2) A single external displacement $(0, \delta)$ of the top nodes is introduced by setting the constraints $u_i^x = 0$ and $u_i^y = \delta \forall i \in \mathcal{T}$.
- 3) This displacement leads to forces acting on all remaining nodes

$$\mathbf{f}_{\text{ext}} = -G \mathbf{u}_{\text{ext}}, \quad (13)$$

where $\mathbf{u}_{\text{ext}} \in \mathbb{R}^{3N}$ is zero everywhere except for the external displacements, i.e., $u_{\text{ext},3 \cdot i+1} = u_i^y$ if $i \in \mathcal{T}$.

- 4) The "glueing" is imitated by enforcing the constraints $u_i^x = 0$ and $u_i^y = 0 \forall i \in \mathcal{B}$. Both the constraints for bottom and top nodes are realized by removing the corresponding rows and columns in the stiffness matrix and the corresponding rows in the external force vector⁷, resulting in their reduced versions \bar{G} and $\bar{\mathbf{f}}_{\text{ext}}$.
- 5) From the reduced stiffness matrix and force vector, we get the displacement of all unconstrained nodes $\bar{\mathbf{u}}$ by solving the following system of linear equations

$$\bar{G} \bar{\mathbf{u}} = \bar{\mathbf{f}}_{\text{ext}}, \quad (14)$$

for instance, by using a linear (and differentiable) solver such as LU decomposition.

- 6) From $\bar{\mathbf{u}}$ and the constraints for top and bottom nodes, the displacement vector \mathbf{u} for all nodes can be constructed.
- 7) From this, we can calculate the full force vector $\mathbf{f} = G\mathbf{u}$.
- 8) The total force of the top nodes pushing upwards is then given by

$$f_{\text{react}} = - \sum_{i \in \mathcal{T}} f_{3 \cdot i+1}, \quad (15)$$

which is turned into a stress by normalizing with the cross-sectional area of the lattice in y-direction, $b_x \cdot \sqrt{A}$,

$$\text{stress} = \frac{f_{\text{react}}}{b_x \cdot \sqrt{A}}. \quad (16)$$

- 9) Finally, we update the node positions of the lattice to their new equilibrium positions $(x_i + u_i^x, y_i + u_i^y)$.

To collect stress values for increasing strain, the whole process is repeated several times. For instance, after two iterations, the total stress is given by the sum of the stresses obtained in both iterations, and the total strain is given by $2 \cdot \delta$. The effective elastic modulus is then obtained via linear regression on the collected total stress values σ and total strain values ϵ ,

$$E^* = \frac{\sum_k \sigma_k}{\sum_k \epsilon_k}, \quad (17)$$

where k sums over all iterations.

⁷I.e., all rows (and columns) $3 \cdot i$ and $3 \cdot i + 1 \forall i \in \mathcal{T} \cup \mathcal{B}$.

This approach can be easily generalized to arbitrary scenarios by defining the sets \mathcal{T} and \mathcal{B} as well as the constraints and external displacements differently.

2) *Calculating the Poisson’s ratio*: To obtain the Poisson’s ratio, the same steps as for the effective elastic modulus are performed. However, instead of the stress, the mean width change $\bar{\epsilon}_k$ is calculated in each iteration k

$$\Delta R = \frac{1}{|\mathcal{RS}|} \sum_{i \in \mathcal{RS}} u_i^x, \quad (18)$$

$$\Delta L = \frac{1}{|\mathcal{LS}|} \sum_{i \in \mathcal{LS}} u_i^x, \quad (19)$$

$$\bar{\epsilon}_k = \Delta R - \Delta L, \quad (20)$$

where \mathcal{RS} is a set containing the indices of all outer-right nodes (i.e., forming the right surface of the material) and \mathcal{LS} the indices of outer-left nodes⁸. $|\mathcal{RS}|$ denotes the number of elements in \mathcal{RS} . For deformations, we neglect the iterations index here to increase the readability. The Poisson’s ratio is then obtained using linear regression

$$\nu^* = \frac{\sum_k \bar{\epsilon}_k}{\sum_k \epsilon_k}. \quad (21)$$

B. Open source package: pyLattice2D

pyLattice2D [32] is a Python package that implements an end-to-end differentiable framework for performing finite element analysis and inverse design of lattice materials in pyTorch. It contains functions for generating a variety of lattices (Square, Equilateral Triangle, Honeycomb, Reentrant Honeycomb, Kagome and Voronoi) with (i) different number of cells and (ii) custom deformations such as node displacements and edge (or node) deletions. In addition, code for training GNNs to predict lattice properties as well as various example notebooks for inverse design problems are included.

In the code, the direct stiffness matrix is constructed in `fem_solver/direct_stiffness.py`, with convenience classes available for setting constraints in `fem_solver/constraints_and_deformations.py`. Code containing the logic for generating different base lattices is in `lattices/`, while the pipeline for dataset generation is in `data/create.py`. The experimental protocol for obtaining the effective elastic modulus and Poisson’s ratio of a lattice is implemented in `methods/mechanical_properties.py`. Wrapped models to be used are found in `models/`, with models/`Lattice.py` implementing the class describing lattices as `graphs`. `models/FEM.py` is the differentiable finite element solver, taking the aforementioned lattice objects as input and performing a single finite element step. `models/MPNN/` contains both GNN models as well as tabular and image-based machine learning models for property prediction. Finally, `Examples/` in the main folder features IPython notebooks with the experiments from this paper, and `Data_Generation` features the Python and Bash scripts used to generate the dataset.

⁸We only use outer nodes that are unconstrained for this calculation.

C. Simulation details

During inverse design, we optimize both the node coordinates \mathbf{r}_i and mask values m_{ij} . However, we only change the coordinates of nodes that are inside of the material, i.e., the outer surface of the material is kept unchanged. For coordinates, we use the learning rate $\gamma_r = 0.001$ and for the edge mask $\gamma_m = 0.01$. If not stated otherwise, we use $\alpha = 1$, $E = 2$ GPa, $b_x = b_y = 1$ cm and $A = 2 \cdot 10^{-5}$ cm² in all simulations. The optimized parameters are not regularized.

For training GNNs, we use a batch size of 200, a learning rate of 10^{-3} (Adam optimizer), weight regularization strength 10^{-6} and a mean squared error loss function. For all trained models, we normalized the values of the effective elastic modulus by first subtracting the minimum value of the training set, and then dividing by the maximum value of the (minimum-shifted) training set.

1) *Inverse design of effective elastic modulus*: In this case, the exact forward model F provides the effective elastic modulus of a given lattice. To determine E^* , F performs 10 iterations of direct stiffness with $\delta = 0.001$, leading to a total compression in height of 0.01 (i.e. 1%). We choose the loss function

$$L_E = \frac{\|F(\mathcal{X}, \mathcal{E}, \mathcal{M}) - E^{\text{target}}\|}{E_0} + \beta \|\bar{\rho} - \bar{\rho}_0\|, \quad (22)$$

where E_0 is the initial effective elastic modulus of the lattice, $E^{\text{target}} = 10 \cdot E_0$ the target value, $\bar{\rho}$ the relative density as obtained using message passing and $\bar{\rho}_0$ the initial relative density. β is a hyperparameter that we choose to be $\beta = 10$.

Masking values are initialized as 0.2 for all edges. No additional edges (beyond regular honeycomb connectivity) are added to the lattice setup. The learning rate for mask values is reduced by a factor of 10 after 40 iterations to guarantee convergence.

2) *Inverse design of Poisson’s ratio*: In this case, the exact forward model F provides the Poisson’s ratio of a given lattice. To determine ν^* , F performs 40 iterations of direct stiffness with $\delta = \frac{0.01}{40}$, leading to a total compression in height of 0.01 (i.e. 1%). We choose the loss function

$$L_\nu = \|F(\mathcal{X}, \mathcal{E}, \mathcal{M}) - \nu^{\text{target}}\| + \beta \|\bar{\rho} - \bar{\rho}_0\|, \quad (23)$$

where $\nu^{\text{target}} = -0.5$ is the target Poisson’s ratio. All other parameters are as in Supplementary Information C1. In addition, the list of crossing beams is recalculated every 10 iterations to ensure a valid lattice material after inverse design has finished.

3) *Inverse design of grabber*: Different from the previous experiments, here the deformation of each node is determined using F , which performs 10 iterations of direct stiffness with $\delta = \frac{0.01}{10}$. For the right outer nodes in the small cavity (Fig. 8, square-shaped nodes in blue), we set as a target that they do not move in x -direction, but move either upwards (lower row) or downwards (upper row) in y -direction by 0.02. Performance is evaluated using an L1 loss again, and we set $\alpha = 100$.

In this experiment, we allow new edges to be added to the lattice that have originally not been part of the honeycomb tiling. Before starting the inverse design loop, we therefore add

new edges (that are masked out initially) to the graph: for each node, edges to neighbouring nodes within a radial distance of 0.2 are added to the graph with a probability of 0.3. Original honeycomb beams (i, j) are initialized with mask value $m_{ij} = 0.25$, while all other (newly added) beams (l, p) are initialized with mask value $m_{lp} = 0$. During inverse design, we also apply the following to promote removing unnecessary beams from the lattice, as well as solutions that are further away from the initial honeycomb structure:

- Every five iterations, the 10% of the active edges (i.e., $\{(i, j) \mid M_{ij} > 0\}$) with the lowest mask value are masked out by setting their mask value to -0.2 .
- Every five iterations, the expressions for M_{ij} are updated by newly checking which beams in the lattice cross. This is done to avoid solutions with crossing beams.

4) *Inverse design of flat surface*: In this experiment, there are two loading scenarios S_1 and S_2 , which we provide as an additional input to the forward model F . More specifically, in the first scenario the four left nodes on the top of the surface are moved downwards, while in the second scenario the four right nodes on the top are moved. In both scenarios, all bottom nodes are kept fixed and the target is to have a flat surface, i.e., the remaining four top nodes have as a target to not move in x -direction and move the same amount in y -direction as the forced nodes.

For training, we again use the L1 loss – however, now it is the sum of the individual losses for both scenarios. Training is done as in Supplementary Information C3, with the only difference being that random masking every five iterations is stopped after 20 iterations.

5) *Dataset generation*: For the dataset, we chose the number of layers N_l in a material using a certain base tiling such that in the end, all lattices were made of approximately the same amount of cells N_c ⁹. The deformations are governed by hyperparameters Δ , D_n and D_e , and we denote by $U(x)$ the uniform distribution over the interval $[0, x]$ ($x \in \mathbb{R}^+$) and $I(N)$ the uniform distribution on integers in the interval $[0, N]$ ($N \in \mathbb{N}$).

To deform a single lattice, maximum values for the deformations are obtained by sampling from random distributions:

$$A_\delta \sim U(1), \quad (24)$$

$$\partial \sim U(\Delta), \quad (25)$$

$$d_e \sim U(D_e), \quad (26)$$

$$d_n \sim I(D_n). \quad (27)$$

The deformations are then applied as follows:

- 1) Select a fraction A_δ of nodes randomly and shift them by a random amount $U(\partial) - 0.5$ both in x and y direction (for both directions, the amount is determined independently).
- 2) Select a fraction d_e of edges randomly and remove them from the edge list (i.e., remove beams from the lattice).

⁹Since all lattices have to fit as best as possible into the unit box, an exact match is impossible.

- 3) Select d_n nodes randomly and remove them as well as all edges connecting to them.

The used values are listed in Table S1. For training, validation and test set, different random seeds were used. This way, a variety of different lattices is generated, with some featuring heavy deformations while others only have small (or localized) deformations.

TABLE S1
PARAMETERS USED FOR DATASET GENERATION.

Lattice type (2D)	N_l	N_c	Δ	D_n	D_e
Square	11	169	0.15	1	0.2
Triangle	14	170	0.15	1	0.2
Honeycomb	25	150	0.05	0	0.2
Reentrant	25	149	0.05	0	0.2

To calculate the effective elastic modulus and Poisson’s ratio, we performed 30 iterations of direct stiffness with $\delta = \frac{0.02}{30}$ on each lattice. A brief summary of the distribution of these values is shown in Fig. S1.

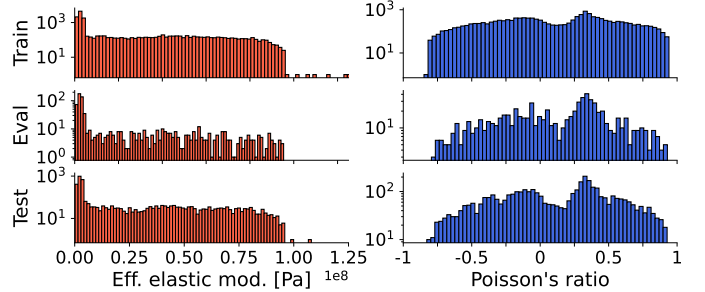


Fig. S1. Distribution of effective elastic modulus and Poisson’s ratio as obtained from our dataset, shown for the different data splits. The abscissas use log-scaling with different ranges.

6) *Training machine learning models*: We train separate models for the effective elastic modulus and the Poisson’s ratio (although in principle, similar performances are reached when training at least the GNN models to predict both properties). For the GNN models, we choose a graph representation with bidirectional edges. In addition, we add a self-connection to each node.

The EdgeConv model consists of three EdgeConv layers (see Eq. (29)) with 200 hidden neurons each. The deep neural network consists of three layers with $[400, 200, 1]$ neurons.

The specification of the MPNN model can be found in pyLattice2D (in `models/MPNN/networks` the class `LatticeNNConv`) with parameters `hid_nfeat` set to 15 and `num_message_passing` set to 3.

For the CNN, we use a batchsize of 50 and weight regularization of 10^{-5} . Training data is randomly flipped horizontally and vertically. The specifications of the CNN architecture can be found in pyLattice2D (in `models/MPNN/networks` the class `CNN`).

7) *Inverse design using GNNs*: For inverse design, we trained an EdgeConv model with 150 hidden neurons per

EdgeConv layer, otherwise the architecture is the same as in Supplementary Information C6. For the inverse design loop, we use again an L1 loss:

$$L_\nu = \|F(\mathcal{X}, \mathcal{E}, \mathcal{M}) - E^{\text{target}}\| + \beta \|\bar{\rho} - \bar{\rho}_0\|, \quad (28)$$

with $\beta = 100$ and F now the trained EdgeConv model. Only original beams of the triangle grid can be added or removed during training. We initialize the mask randomly with values $m_{ij} \sim U(0.2)$, which was necessary to avoid that the model removes too many beams at once during the first few iterations. For coordinates, we use the learning rate $\gamma_r = 0.0001$ and for the edge mask $\gamma_m = 0.001$. All parameters are regularized (weight decay) with strength 10^{-6} .

For comparison, we use an exact forward model (FE in Fig. 12) which uses 10 iterations of direct stiffness with $\delta = 0.002$ to determine E^* .

D. Machine learning models

1) *Graph neural networks*: We investigate graph neural networks that work directly on the graph structure of our lattices, using only the information contained in \mathcal{L} .

Here, we use the EdgeConv model [45], where the node features \mathbf{r}_i are updated as follows:

$$\mathbf{r}_i^{(l+1)} = \max_{j \in \mathcal{N}_i} \left(W (\mathbf{r}_j^{(l)} - \mathbf{r}_i^{(l)}) + W_0 \mathbf{r}_i^{(l)} \right), \quad (29)$$

with $\mathbf{r}_i^{(0)} = \mathbf{r}_i$. The full model consists of several EdgeConv, followed by a dense deep neural network Φ that returns a property prediction for each node. The final prediction is then obtained by averaging over all nodes.

In addition, we investigate the MPNN model that has been proposed for molecule property prediction [41]. For this model, we use the distance vector between nodes \mathbf{r}_{ij} , the length of the beam L_{ij} as well as the orientation c_{ij} as edge features $\mathbf{e}_{ij} = (\mathbf{r}_{ij}, L_{ij}, c_{ij})$. Node features are first preprocessed using a multi-layer neural network ϕ_r . They are update using a NNConv layer and a gated recurrent unit (GRU)

$$\tilde{\mathbf{r}}_i = \mathbf{r}_i^{(l)} + \text{mean}\{\phi_e(\mathbf{e}_{ij}) \cdot \mathbf{r}_j^{(l)}, j \in \mathcal{N}_i\}, \quad (30)$$

$$\left(\mathbf{r}_i^{(l+1)}, \mathbf{h}_i^{(l+1)} \right) = \text{GRU} \left(\tilde{\mathbf{r}}_i, \mathbf{h}_i^{(l)} \right), \quad (31)$$

with $\mathbf{r}_i^{(0)} = \mathbf{h}_i^{(0)} = \phi_r(\mathbf{r}_i)$ and where ϕ_e is a neural network that takes the edge features as input and returns a matrix. This step is repeated N times, after which a graph embedding \mathbf{r}_g is obtained by pooling over all nodes

$$\mathbf{r}_g = \text{pool} \left(\left\{ \mathbf{r}_0^{(N)}, \dots, \mathbf{r}_{|C|}^{(N)} \right\} \right). \quad (32)$$

For pooling, we use the Set2Set operator. From \mathbf{r}_g , a prediction is obtained through a final multi-layer neural network ϕ_p .

2) *Tabular models*: For comparison, we consider both linear regression and gradient-boosted trees (CatBoost). Such models work best with engineered features that summarise the characteristics of a lattice \mathcal{L} . In addition to the graph representation of the lattice, we also use its image representation \mathcal{I} here, which is given by a matrix $\mathcal{I} \in \{0, 1\}^{c_0} \times \{0, 1\}^{c_1}$, with

$c_0 \times c_1 = 339 \times 459$ being the image resolution and a value of 1 indicating the existence of lattice material. Here, we use the following features:

TABLE S2
PARAMETERS FOR THE DATASET GENERATION.

Tiling	
Image mean	$\text{mean}(\mathcal{I})$
Image standard deviation	$\text{std}(\mathcal{I})$
Relative density	$\bar{\rho}$
Beam length mean	$\text{mean}(L)$
Beam length standard deviation	$\text{std}(L)$
Beam length minimum	$\min(L)$
Beam length maximum	$\max(L)$
Cell area mean	$\frac{1 - \text{mean}(\mathcal{I})}{N_c}$
Cell area standard deviation	$\frac{\text{std}(1 - \mathcal{I})}{N_c}$

$N_c = N_b - N_n + 1$ is the number of closed cells in the lattice, N_b the number of beams and N_n the number of nodes.

3) *Masking EdgeConv*: For EdgeConv, message passing yields the following edge features for each edge (j, i)

$$E_{ji} = \left(W (\mathbf{r}_j^{(l)} - \mathbf{r}_i^{(l)}) + W_0 \mathbf{r}_i^{(l)} \right). \quad (33)$$

Masking is done as follows:

$$E_{ji} \leftarrow E_{ji} \cdot M_{ji} + \min_{n,m} (E_{nm}) \cdot (1 - M_{nm}). \quad (34)$$

Node features are updated by choosing the maximum value (element-wise) over all neighbouring edges

$$\mathbf{r}_i^{(l+1)} = \max_{j \in \mathcal{N}_i} (E_{ji}). \quad (35)$$

Hence, if an edge is masked, its value is not picked by the max operation and it appears as if the edge does not exist in the graph. The masking also guarantees that the chosen maximum value cannot be larger than the minimum value of the edge features, always guaranteeing that the masked value is not chosen by accident. If the graph is bidirectional, both forward and backward edge between two nodes are masked with the same mask value, i.e., $m_{ji} \equiv m_{ij}$, resulting in $M_{ji} \equiv M_{ij}$. Self-connections (i, i) in the graph are not masked¹⁰.

E. Supplementary figures

1) *Inverse design of flat surface*: During training, we only used a single external deformation δ . Fig. S2 shows that – even though we only trained on this singular point of the deformation – since we are operating in the linear regime of the material, the target behaviour is also satisfied for weaker and stronger loads.

¹⁰This also guarantees that masking still works if nodes become disconnected from the remaining graph.

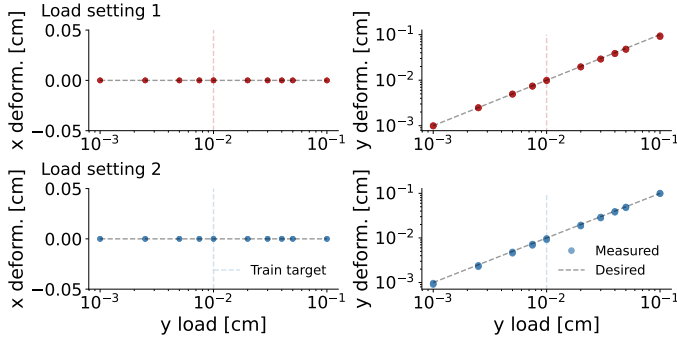


Fig. S2. Target deformation (horizontal dashed line) and observed deformation (dots) for different absolute load strengths. Even for loads that are much lower or higher than the one used for training (vertical dashed line), the found lattice material obeys the desired target behaviour.

2) *Inverse design using a graph neural network*: Comparison of the found lattice design with the two training examples that resemble it most. Similarity is calculated using the image representation of a lattice. The 2D image of the generated lattice design is denoted by \mathcal{I}_{GNN} , while the images of the lattices in the training dataset are denoted by \mathcal{I}_i . Dissimilarity Δ_s is calculated using

$$\Delta_{s1}(\mathcal{I}_{\text{GNN}}, \mathcal{I}_i) = \frac{\text{mean}((\mathcal{I}_{\text{GNN}} \vee \mathcal{I}_i) \wedge \mathcal{I}_{\text{GNN}})}{\text{mean}(\mathcal{I}_{\text{GNN}})}, \quad (36)$$

$$\Delta_{s2}(\mathcal{I}_{\text{GNN}}, \mathcal{I}_i) = \frac{\text{mean}((\mathcal{I}_{\text{GNN}} \vee \mathcal{I}_i) \wedge \mathcal{I}_i)}{\text{mean}(\mathcal{I}_i)}, \quad (37)$$

$$\Delta_s(\mathcal{I}_{\text{GNN}}, \mathcal{I}_i) = \Delta_{s1}(\mathcal{I}_{\text{GNN}}, \mathcal{I}_i) + \Delta_{s2}(\mathcal{I}_{\text{GNN}}, \mathcal{I}_i) \quad (38)$$

where mean calculates the mean over all pixels and we treat Boolean values as integers (False – 0; True – 1) when taking the mean. The two lattices in the training dataset with the lowest dissimilarity are shown in Fig. S3.

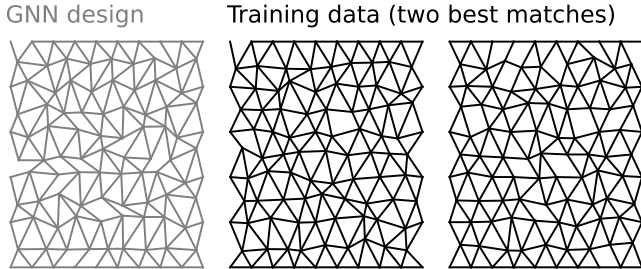


Fig. S3. Images of the two lattices in the training set that resemble the found design most.